Check for updates

Proceedings of ASME Turbo Expo 2026
Turbomachinery Technical Conference and Exposition
GT2026
June 15-19, 2026, Milan, Italy

GT2026-175529

Downloaded from asmedigitalcollection.asme.org/GT/proceedings-pdf/GT2026/89817/V011T34A011/7650378/v011t34a011-gt2026-175529.pdf by Deutsches Zentrum für Luft- und Raumfahrt (DLR) user on 20 November 2026

A MULTI-DISCIPLINARY MISSION-ORIENTED PRE-DESIGN PROCESS FOR TURBINE BLADE COOLING SYSTEMS

Francisco Carvalho[1,*], **Patrick Wehrel**[2], **Meiken Patzer**[3], **Robin Schöffler**[1], **Clemens Grunwitz**[1], **Julie Frank**[1], **Robin G. Brakmann**[1], **Florian Herbst**[4]

[1]DLR, Institute for Propulsion Technology, Turbine Department, Göttingen, Germany
[2]DLR, Institute for Propulsion Technology, Engine Department, Cologne, Germany
[3]DLR, Institute of Structures and Design, Component Design and Manufacturing Technologies Department, Stuttgart, Germany
[4]DLR, Institute for Propulsion Technology, Cologne, Germany

ABSTRACT

Turbine cooling pre-design methods often require conservative safety margins that can lead to excessive cooling and specific fuel consumption (TSFC). This work presents a holistic, multi-point pre-design methodology that integrates aerothermal and structural considerations to more accurately dimension turbine cooling systems and reduce design conservatism. The workflow spans engine, turbine, and airfoil scales. A zero-dimensional engine model supplies boundary conditions to meanline and through-flow solvers, where a semi-empirical model provides an initial sizing of the cooling system. Each cooled row is then resolved into hub, mid, and tip radial sections. For each operating point in the flight envelope, blade aerodynamics along with blade thermal and structural performance are accounted for when optimizing the cooling system. Finally, with a bi-directional coupling between the different modeling levels, we are able to quantify the impact of coolant requirement changes at turbine and engine level. This process is applied to a representative turbofan high-pressure turbine with a focus on the first blade. Its cooling system is dimensioned by various multi-disciplinary constraints that appear throughout the flight envelope, not only at maximum take-off conditions. For the case in question, enforcing these constraints in a multi-point cooling system design drives up the coolant requirements by 16.2% in comparison to a single-point design before safety margins are applied, but also reduces uncertainty.

Keywords: Turbine, Cooling, Pre-design, Multi-point

NOMENCLATURE

A	Area
c_p	Isobaric specific heat capacity
c	Velocity
E	Young's modulus
h	Specific enthalpy
$\dot{m}$	Mass flow rate
P	Power
q	Quasi-normal coordinate
r	Radius
R	Stage reaction, thermal resistance
T	Temperature
p	Pressure
u	Blade circumferential velocity
w	Specific work
t_r	Rupture time
D	Damage
α	Coefficient of thermal expansion
γ	Local flow angle, stagger angle, specific heat ratio
δ	Angle between quasi-normal and radial direction, wall thickness
ε	Emissivity
ε_0	Cooling effectiveness
ε_f	Film cooling effectiveness
η_c	Cooling efficiency
λ	Thermal conductivity
ν	Poisson ratio
ρ	Density
σ	Stefan–Boltzmann constant, Stress
η_{Ts}	Turbine isentropic efficiency
ϕ	Injection angle, flow coefficient
Ψ	Loading coefficient
Re	Reynolds number
St	Stanton number
Bi	Biot number

Subscripts

1, 2	Blade inlet, blade outlet
u	Circumferential

*Corresponding author: francisco.carvalho@dlr.de

Copyright © 2026 by ASME; reuse license CC-BY 4.0

ax	Axial
m	Meridional, metal
coat	Coating
c	Coolant
g	Gas
aw	Adiabatic wall
i, o	Inlet, Outlet
rel	Relative frame
s, vs	Surface, Visible surface
t	Total
vM	von Mises
conv, rad	Convective, Radiative
∞	Mainstream conditions

Abbreviations

ADP	Aerodynamic Design Point
CHT	Conjugate Heat Transfer
EOF	End of Field
HLP	Heat Load Parameter
HPT	High-Pressure Turbine
LMP	Larson–Miller Parameter
MP	Multi-Point
MTO-SLS	Maximum Take-Off Sea-Level-Static
OP	Operating Point
PF	Pattern Factor
PR	Pressure Ratio
SF	Scaling Factor for row coolant, Safety Factor
SP	Single-Point
SLC	Streamline Curvature
SCF	Stress Concentration Factor
S2m	Meridional (x–r) plane
TO	Take-Off
TOC	Top of Climb
YS	Yield Strength
TSFC	Thrust Specific Fuel Consumption

1. INTRODUCTION

High-pressure turbines (HPTs) in aero-engines operate at gas temperatures well above the melting point of typical Ni-based superalloys [1]. Increasing the turbine inlet temperature is a primary lever for improving cycle efficiency and reducing thrust-specific fuel consumption (TSFC) [2, 3], but only up to a certain point. Higher coolant needs can lead to excessive losses at turbine and engine level, with a negative net profit [4, 5]. The design of the cooling system is therefore a critical enabler for fuel burn savings. Apart from novel cooling and material technologies, lowering uncertainties in the cooling system design can also generate savings. On the one hand this enables a more aggressive design with reduced safety margins and coolant mass flow. On the other hand, reduced uncertainties facilitate more robust designs with extended component lifetime and engine time on wing, reducing the need for hot-section maintenance programs [6–8] later on. In this paper, we lower these cooling design uncertainties by using an efficient iterative pre-design process between engine, turbine and airfoil that accounts for aerodynamic, thermal and structural aspects of the cooling system throughout the flight envelope.

It is typical for studies on turbine cooling systems to adopt a one-way information flow from engine to airfoil. Studies at engine and turbine level often do not get feedback from the airfoil level and must resort to reduced cooling models as a replacement. These can be purely empirical [9, 10] or indeed have a physical background (semi-empirical) [11–13]. It is an efficient and widely adopted approach in the literature [14–24] that lets us investigate the impact of different material or cooling technologies at system level. Despite its upsides, this approach averages the airfoil into one point and cannot resolve local challenges such as critical pressure ratios, stress or temperature peaks. Airfoil level studies on the other hand are typically prescribed boundary conditions from the engine or turbine level that are not updated when the airfoil cooling design changes [25–28]. This airfoil level research provides detailed insight into cooling efficiency, metal temperatures or local life consumption, but the impact of the resulting cooling design on system performance is usually only discussed qualitatively. Explicit bi-directional coupling between airfoil and system level modeling remains the exception rather than the rule. Less cooling at a particular position is not always better [4, 5], so that this feedback loop is critical to understand which technologies applied to which position in the turbine provide a net benefit at engine and aircraft level. An exciting solution is to connect the engine and the turbine level modeling with a higher detail thermal model for each turbine row to get a direct feedback - a zooming process. *Woelki and Peitsch* [29] and *Schuff* [30] implemented this two-way information flow, but with a focus on the secondary air system (SAS). Specifically for the airfoil cooling system, *Yin* [31] combined a one-dimensional cooling model with a turbine model to investigate how prescribed cooling configurations affect engine efficiency. This last development moves towards a more holistic design of the turbine cooling system, but such approaches are scarce in the literature.

Furthermore, the cooling system is typically dimensioned in the literature for a small set of high-load operating points, maximum take-off sea-level static (`MTO-SLS`) and occasionally maximum climb (`MCL`). Several engine level studies dimension the cooling system for `MTO-SLS` with both empirical and semi-empirical models [18–23]. A few additional studies, from *Ziegler et al.* [24] and *Schröter et al.* [32] for a hybrid regional aircraft engine and for the WET engine, take additionally `MCL` as a dimensioning point. A similar trend is visible at airfoil level studies, where the analysis and optimization of a cooling system is mostly focused on a single operating point [33–37], often `MTO-SLS`. In short, dimensioning and optimizing the cooling system for the entire flight envelope is, to our knowledge, currently not practiced in the literature. An *a posteriori* analysis of an airfoil cooling system throughout the flight envelope does exist in the literature, but generally under the assumption of a fixed cooling configuration and with a focus on identifying major damage sources and evaluating damage accumulation [38–40]. Thus, the flight envelope and any one flight cycle is mostly used as an input for damage prediction for a fixed cooling design rather than as a driver for the design of the cooling system itself.

The toolkit and pre-design process described in this study address the identified gaps in the literature in three key ways. First, by coupling engine, turbine and airfoil modeling in an iterative process. This allows us to quantify and understand the impact of a cooling design at system level. Second, by integrating both

Downloaded from asmedigitalcollection.asme.org/GT/proceedings-pdf/GT2026/89817/V011T34A011/7650378/v011t34a011-gt2026-175529.pdf by Deutsches Zentrum für Luft- und Raumfahrt (DLR) user on 20 November 2026

Copyright © 2026 by ASME; reuse license CC-BY 4.0

thermal and structural performance into the airfoil level cooling system pre-design. This provides the grounds for a fair comparison between different cooling designs, especially when applying different material technologies with different mechanical properties. And third, by including the entire flight envelope in the airfoil level cooling system pre-design. With this, we can reduce uncertainties in the design process to arrive at either a more aggressive or a more robust airfoil cooling system.

While beneficial for standard civil aviation, this approach is critical for high-performance platforms characterized by wider and more demanding flight envelope and flight cycles, as would be the case of supersonic commercial transport or aerial firefighting. After discussing the individual elements of this toolkit, we apply it to a geared turbofan HPT blade to demonstrate the workflow and highlight dimensioning aspects for the airfoil cooling system throughout the flight envelope.

2. METHODS

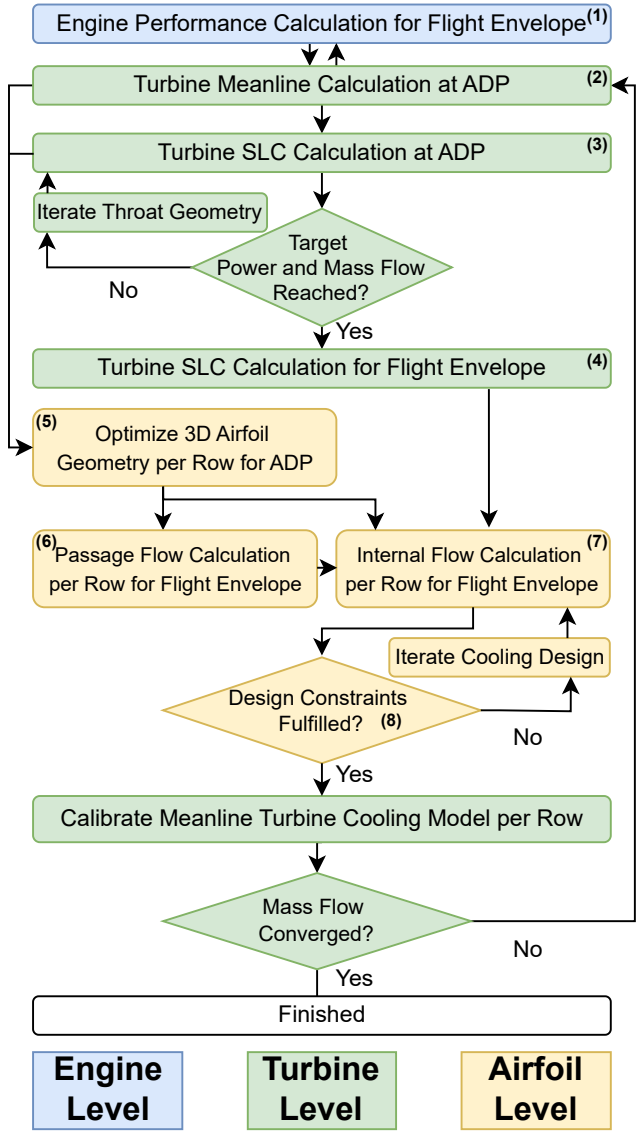

FIGURE 1: Connection between modeling levels.

Figure 1 serves as a visual aid throughout this section, providing a brief overview of how the individual tools are connected to one another. The pre-design toolkit proposed by *Grunwitz et al.* [41] has been extended in this paper in three key ways, as discussed in the previous section. First, the turbine model is iterated with the airfoil model for each turbine row, between steps 2 and 7 from Fig. 1, until convergence is achieved. Second, the thermal optimization of the airfoil cooling system has been extended with a structural component in step 7. The design constraints from step 8 have been extended accordingly and are discussed in Sec. 3. Third, a single-point design approach has been replaced by a multi-point approach, in steps 4, 6 and 7, that takes the complete flight envelope into account.

Starting at step 1, all operating points are calculated at engine level based on thrust requirements iterated between engine and aircraft modeling. The flow state at the turbine inlet in the engine model is passed down to the turbine model as a boundary condition, along with power delivery and shaft-speed. An initial turbine geometry is first generated and optimized for an aerodynamic design point (ADP) using a meanline tool and a streamline curvature tool (SLC). The turbine flow is then computed with the SLC tool for all operating points in the flight envelope. At airfoil level, the profile of each row is optimized with an Euler solver for pressure losses at three radial sections, hub, mid and tip, within the geometrical constraints and flow boundary conditions set by the turbine meanline and SLC calculation. Finally, the modeling of the internal cooling system requires input from the SLC model for the row inlet boundary conditions, from the passage flow calculation with the Euler solver for the Mach number distribution over the airfoil and finally from the actual three-dimensional shape of the airfoil. The cooling system is then optimized and finally provides input per cooled turbine row to the cooling model integrated in the turbine meanline calculation. Once mass flow converges, the meanline turbine is coupled with the engine model and re-iterated.

2.1 Engine Level Analysis

The engine cycle is evaluated with a zero-dimensional performance model [42] as shown in Fig. 2. Multi-stage turbines are handled as equivalent single-stage elements and modeled through performance maps. Cooling air is extracted at predefined compressor stations and routed through the secondary-air-system (SAS). Off-design performance is obtained by iterating mass flow and shaft speeds until all component maps and power balances are satisfied. The engine model is tightly coupled with the turbine meanline model exchanging turbine inlet conditions, work, efficiency, and coolant mass flow until convergence is achieved. This ensures consistent boundary conditions for the subsequent turbine and cooling system pre-design steps.

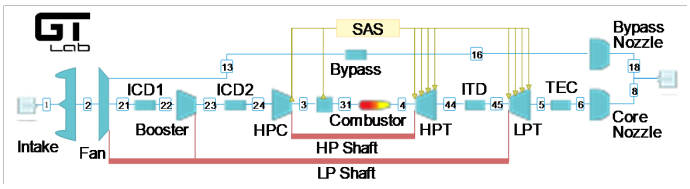

FIGURE 2: Performance model of a geared turbofan engine [43–45] in GTLab.

Downloaded from asmedigitalcollection.asme.org/GT/proceedings-pdf/GT2026/89817/V011T34A011/7650378/v011t34a011-gt2026-175529.pdf by Deutsches Zentrum für Luft- und Raumfahrt (DLR) user on 20 November 2026

Copyright © 2026 by ASME; reuse license CC-BY 4.0

2.2 Turbine Level Analysis

2.2.1 Meanline Modeling. The meanline turbine model [46, 47] is based on a reduced set of requirements provided by the engine model, such as power, shaft-speed, inlet mass flow along with turbine inlet and coolant flow state. Spool specific work is calculated from the target power and the rotor inlet mass flow. Stage number is automatically adjusted to keep the loading of any stage (Eq. 1) below a user defined limit.

$$\Psi = \frac{w}{u^2} = \frac{c_{1u} - c_{2u}}{u}, \tag{1}$$

$$\phi = \frac{c_{ax}}{u}, \tag{2}$$

$$R = 1 - \frac{c_{2u} + c_{1u}}{2 \cdot u}. \tag{3}$$

For each turbine row, the airfoil number is estimated from empirical correlations [48, 49]. The axial velocity components are defined by the mass flow and the flow coefficient. The latter is calculated from Eq. 2 where both c_{ax} and u are averaged between stations 1 and 2. The blade inlet tangential velocity component is calculated from stage reaction and loading with Eq. 1 and Eq. 3. And finally, the blade outlet tangential velocity component is calculated through the *Euler* work equation to deliver the target power. Pressure losses are calculated for each row according to Sec. 2.2.3. In addition to the meanline calculation, a radial flow distribution is modeled by prescribing a twist law for the tangential velocity followed by a simple radial equilibrium formulation for the axial velocity [3]. With this, the meanline turbine model can deliver the two-dimensional geometry input required by the through-flow turbine model from Sec. 2.2.2.

The cooling system is dimensioned per turbine row using a derivation of the model proposed by *Holland and Thake* [11, 12], already applied in [5]. The relative coolant mass flow is given by

$$\dot{m}_{c,rel} = \frac{c_{p,g}}{c_{p,c}} \cdot \frac{A_s}{A_g} \cdot St_g \cdot HLP, \tag{4}$$

with the heat load parameter HLP defined as $HLP = HLP_{conv} + HLP_{rad}$. The convective and the radiative components are shown in Eq. 5 and Eq. 6.

$$HLP_{conv} = \frac{\varepsilon_f \cdot (1 - \eta_c) + \varepsilon_0 \cdot (\varepsilon_f \cdot \eta_c - 1)}{\eta_c \cdot (\varepsilon_0 - 1)} \cdot \frac{1}{1 + Bi_{coat}} \tag{5}$$

$$HLP_{rad} = 0.5 \cdot \sigma \cdot (1 + \varepsilon_s) \cdot \varepsilon_g \cdot \frac{\varepsilon_0}{2 \cdot h_g \cdot \eta_c} \cdot T_{t,g}^3 \cdot \left[1 + \frac{T_s}{T_{t,g}} + \left(\frac{T_s}{T_{t,g}} \right)^{1.5} \right] \cdot \cos\gamma \tag{6}$$

with

$$\eta_c = \frac{T_{t,c,o} - T_{t,c,i}}{T_m - T_{t,c,i}}, \quad \varepsilon_f = \frac{T_{t,g} - T_{t,aw}}{T_{t,g} - T_{t,c,o}}, \quad \varepsilon_0 = \frac{T_{t,g} - T_m}{T_{t,g} - T_{t,c,i}}. \tag{7}$$

The modeled coolant requirement is for the airfoil only. Row coolant mass flow is obtained from Eq. 8 with SF values currently based on empirical data from the NASA E3 turbines [50, 51].

$$SF = \frac{\dot{m}_{c,row}}{\dot{m}_{c,airfoil}} \tag{8}$$

In the meanline turbine model, the effect of combustor hot-streaks on the cooling requirements is modeled through a scalar pattern factor PF that is calculated from literature based combustor exit temperature profiles [52]

$$PF = \frac{T_{t,g,max} - T_{t,g}}{T_{t,g} - T_{t,c,i}}. \tag{9}$$

2.2.2 Streamline Curvature Modeling. The through-flow solver [53] follows the classical streamline–curvature (SLC) formulation from *Denton and Came* [54], computing the meridional flow field of an axial turbine by enforcing mass, momentum, and energy conservation along stream-tubes while coupling neighboring streamlines through a radial equilibrium equation. All quantities are circumferentially averaged, resulting in a two-dimensional system in the S2m plane (x-r plane).

In the unbladed duct regions, the solver advances from axial stations $i - 1$ to i using the conservation laws for mass, angular momentum and enthalpy. Across the bladed region, the solver enforces mass and rothalpy conservation to determine throat and exit conditions. Pressure losses are computed with the empirical correlations from Sec. 2.2.3. The coupling between adjacent streamlines is then achieved by solving the radial equilibrium equation along quasinormals

$$\frac{1}{\rho} \frac{dp}{dq} = \frac{c_u^2}{r} \cos\delta - \frac{c_m^2}{r_c} \cos(\gamma - \delta), \tag{10}$$

where q is the quasi-normal direction, γ is the local flow angle, r_c is the streamline curvature radius, and δ is the angle between the quasi-normal direction and the radial direction.

At each iteration, the solver then updates the static pressures and mass flows at each row exit, and adjusts the radial positions of streamlines to ensure equal mass flow in every stream-tube (Eq. 11). Convergence is reached when mass flows and streamline positions are consistent across all stations and stream-tubes.

$$A_{new} = \frac{\dot{m}_{target}}{\dot{m}} A_{old} \tag{11}$$

Here the effect of combustor hot-streaks is modeled through a literature-based radial temperature profile derived from combustor exit temperature profiles [52].

2.2.3 Pressure Loss Modeling. The pressure loss estimation is consistent between the meanline and the stream curvature methods and includes profile, trailing edge, secondary flow, tip clearance and mixing loss components. Profile losses are evaluated using a formulation that follows the classical approach of *Ainley and Mathieson* [48], but extended by the Mach number dependent terms of *Kacker and Okapuu* [55], the Reynolds number correction from *Zhu and Sjolander* [56] and the supersonic expansion term from *Aungier* [57]. Trailing-edge losses are computed from kinetic-energy loss coefficients extracted from *Ainley*

Downloaded from asmedigitalcollection.asme.org/GT/proceedings-pdf/GT2026/89817/V011T34A011/7650378/v011t34a011-gt2026-175529.pdf by Deutsches Zentrum für Luft- und Raumfahrt (DLR) user on 20 November 2026

Copyright © 2026 by ASME; reuse license CC-BY 4.0

and Mathieson and combined with the isentropic kinetic-energy deficit formulation of *Kacker and Okapuu*. Secondary losses are evaluated with the correlation of *Benner and Sjolander* [58] and tip clearance losses follow the formulation from *Ainley and Mathieson*. Finally, the momentum–mixing losses generated by coolant injection are estimated with the *Hartsel* [59] mixing-layer formulation, based on the coolant-to-gas mass fraction, the relative velocity ratio and the injection angle. As shown in Eq. 12, mixing losses increase with higher coolant requirements and motivate the need for less coolant at turbine level performance.

$$Y_{\text{mix}} = \frac{\gamma}{2} \cdot \text{Ma}_g^2 \cdot \frac{\dot{m}_c}{\dot{m}_g} \left[1 + \frac{T_{t,c}}{T_{t,g}} - 2 \cdot \frac{c_c}{c_g} \cos(\phi) \right] \tag{12}$$

2.3 Airfoil Level Analysis

The airfoil modeling is split into three radial sections, hub, mid and tip, and relies on the two-dimensional flow field provided by the SLC turbine model. For each turbine row inlet and outlet, a radial distribution is extracted from the S2m plane (x-r plane) flow field solution of the SLC simulation. Both the airfoil profile and the cooling system design can then be manually iterated by the user or coupled with a multi-objective optimizer [60].

2.3.1 Airfoil Profile Modeling. The passage flow at each radial section is computed with `MISES`, a two-dimensional viscous–inviscid interaction solver [61] that calculates the flow on the S1 blade-to-blade stream surface (m-θ' plane) by coupling an inviscid passage solution with boundary-layer and wake models, so that possible separation, shock–boundary-layer interaction and profile losses are captured at low computational cost. The code accounts for compressibility and supports both subsonic and transonic regimes. In practice, this solver is used to evaluate and optimize the aerodynamic performance of each radial profile. Finally, as input for the internal cooling system design, we extract a Mach number distribution over each of the three profiles and generate a three-dimensional airfoil by stacking them.

This solver neglects three–dimensional effects such as secondary flows, radial transport of mass and momentum and end-wall–induced loss mechanisms. These simplifications make it well suited for pre-design studies between different cooling designs with a constant external airfoil profile, but inherently limit predictive capability of three–dimensional aerodynamic performance.

2.3.2 Airfoil Cooling System Modeling. The cooling system modeling is split into three radial sections, hub, mid and tip for a correlation based analysis [34]. The input from Sec. 2.3.1 is combined with the hot gas and coolant total pressure and temperature data extracted from the SLC model for the relevant turbine row. A volume is then generated for each internal chamber based on the external airfoil profile and on the thickness of exterior and internal walls. Combining the radial sections with the internal walls along the camber-line, a matrix with nodes is formed. Adjacent nodes in this matrix can be connected to define any desired flow path, as in Fig. 7b. Each node is assigned an internal cooling method, whether it be impingement cooling, ribbed channels or smooth channels, based on which the corresponding correlations for heat transfer and pressure loss are applied. Film cooling holes or slots are then applied to reintroduce the coolant into the main stream. Both the internal cooling and the film cooling features are parameterized and can thus be optimized. This includes rib configurations, pin diameters and spacing in the trailing edge as well as impingement hole layouts. The correlation based internal and external heat transfer coefficients, combined with the material properties and wall thickness, define the through-wall heat flux from Eq. 13 for each cell of each section along the chord-wise direction. This is then used to calculate a through-wall temperature gradient.

$$\dot{Q} = \frac{T_\infty - T_c}{R_{\text{ext}} + R_{\text{coat}} + R_{\text{metal}} + R_{\text{int}}}, \tag{13}$$

$$R_{\text{ext}} = \frac{1}{h_g \cdot A_{\text{ext}}}, \tag{14}$$

$$R_{\text{coat}} = \frac{\delta_{\text{coat}}}{\lambda_{\text{coat}} \cdot A_{\text{ext}}}, \tag{15}$$

$$R_{\text{metal}} = \frac{\delta_{\text{metal}}}{\lambda_{\text{metal}} \cdot A_{\text{ext}}}, \tag{16}$$

$$R_{\text{int}} = \frac{1}{h_c \cdot A_{\text{ext}}}. \tag{17}$$

The matrix model exchanges mass, pressure, and temperature information between nodes, accounting for coolant heating and internal pressure losses. The pressure field is updated by computing cumulative pressure losses along each flow path. Then, the total pressure at each node is obtained using the known coolant supply pressure. Next, the coolant mass flow rate is updated by summing the discharged flows from downstream nodes in reverse flow direction to determine the upstream coolant mass flow rate and ultimately the total inlet coolant mass flow rate. The coolant total temperature is updated for each node based on the surface area to an outer wall and the computed through-wall heat fluxes, so that it continuously increases along the flow path. Coolant and material properties are updated at each iteration based on the flow state of each matrix node and the temperature of each wall cell. The procedure is repeated until mass, momentum, and energy converge.

The temperature distribution calculated with this thermal model serves as input for a cell-wise stress estimation. A subsequent analysis based on the von Mises stress, von Mises safety factor and creep damage per operating point is used to evaluate the structural performance of the cooled blade. We assume positive tensile and negative compressive stress.

Thermal stresses are decomposed into bi-axial and radial in–plane components. The bi-axial stress component idealises the airfoil as a flat plate with fixed edges as in [62]

$$\sigma_{\text{th,bi-ax}} = \frac{\Delta T \cdot \alpha \cdot E}{2 \cdot (1 - \nu)}, \tag{18}$$

where ΔT is the through-wall temperature difference, α the coefficient of thermal expansion, E the Young modulus and ν the Poisson ratio. Unable to deform, the hotter side of the wall experiences compressive and the colder side tensile stress.

The temperature of each cell is then compared to the section average metal temperature to approximate a radial thermal stress component according to *Kerrebrock* [63]

Copyright © 2026 by ASME; reuse license CC-BY 4.0

Downloaded from asmedigitalcollection.asme.org/GT/proceedings-pdf/GT2026/89817/V011T34A011/7650378/v011t34a011-gt2026-175529.pdf by Deutsches Zentrum für Luft- und Raumfahrt (DLR) user on 20 November 2026

$$\sigma_{\text{th,rad}} = E \cdot \alpha \cdot (\overline{T} - T), \tag{19}$$

so that regions with metal temperatures higher than $\overline{T}$ experience radial compression.

Finally, centrifugal loading is evaluated for each radial section of the airfoil. It is integrated between each section and the blade tip, accounting for radius and cross-sectional area variation. This mechanical stress component is superposed on the thermal bi-axial and radial stress components. Assuming an isotropic behaviour for Ni-based superalloys, the stress state is reduced to an equivalent von Mises stress [64]. This is used to estimate both instantaneous stress margins and creep life.

Film-cooling holes are represented at structural level through scalar stress-concentration factors (SCF) applied to the von Mises stress in all cells containing a hole outlet. A distinction is made between an elastic SCF for instantaneous checks and a reduced creep SCF for long-term creep assessment. An elastic SCF value of 1.7 is consistent with detailed numerical and experimental studies of single-crystal alloys with multi-row film-cooling holes [65]. A reduced creep SCF value of 1.3 is a modeling choice guided by the observation that local stresses at notches relax significantly under long-term creep loading in Ni-based superalloys [66].

The von Mises safety factor in each cell is finally defined as the ratio of the temperature-dependent yield strength YS to the von Mises stress including the elastic SCF

$$\text{SF}_{\text{vM}} = \frac{\text{YS}}{\sigma_{\text{vM}}}. \tag{20}$$

Creep life is estimated cell-wise using the Larson–Miller parameter (LMP), which correlates stress, operating temperature and rupture time [67]. With the available information on temperature and stress at each cell, we obtain a material-specific LMP value from which rupture time t_r can be calculated by inverting

$$\text{LMP} = T \cdot \left(\log_{10} t_r + 20\right). \tag{21}$$

For any given operating point with flight time Δt_{OP}, the creep damage in each cell is computed using a linear life-fraction rule

$$D_{\text{OP}} = \frac{\Delta t_{\text{OP}}}{t_{r,\text{OP}}}. \tag{22}$$

This is mathematically analogous to the Palmgren–Miner linear damage rule originally formulated for fatigue [68], and corresponds to the time-fraction approach commonly employed in conventional creep lifing methods [69, 70]. Summing D_{OP} over all operating points of the flight cycle in question delivers the total damage per cell, and the corresponding equivalent mission life with $N_{\text{cell}} = 1/\sum_{\text{OP}} D_{\text{cell,OP}}$. The blade global equivalent mission life is derived as the mean life of the lowest 1% (1st-percentile) of the cell life distribution.

This airfoil cooling system modeling is not yet capable of resolving the heat transfer between the suction and pressure side of the airfoil through internal walls or through the trailing edge. Furthermore, radial heat transfer between sections is accounted for through the coolant heating along its flow path, but not through the wall. These aspects play a role both in the analysis of the thermal and structural performance. In particular for the structural modeling, by not spatially resolving the connection between suction and pressure side at the trailing edge and at the internal walls, we may overlook critical stress regions that will not be optimized for. Addressing these limitations constitutes a part of the future development work planned in this toolkit.

2.4 Validation

Each component of the modeling tools discussed above has been incrementally validated over time with both experimental and high-fidelity numerical studies [16, 47, 53, 71–73]. The discussion below focuses on one particular validation case between our modeling tools and the NASA E3 GE HPT first stage [50]. At turbine level, we see a comparison between general performance parameters in Tab. 1, with the output parameters additionally listed with a relative deviation to the literature values. The meanline turbine model reproduces the literature performance quite well in terms of loading with a slight over-estimation of the pressure losses, visible through the increased pressure ratio. The SLC turbine model also shows an over-estimation in pressure losses, but in addition, a reduced power delivery that ultimately affects the loading coefficient. This may be a result of the underestimated flow turn through the blade in the SLC turbine model, visible in Fig. 3. The Mach number radial distribution shows a good agreement at vane outlet and blade inlet, with a larger deviation at the blade outlet. Furthermore, there is a noticeable reduction in the Mach number towards the hub and tip for both the vane and the blade outlet in the SLC turbine model. This may be caused by how the cavity seal coolant is added to the mainstream flow. A larger deviation is visible in the stage reaction, which may be more related to the definition than to flow physics. While the meanline turbine model uses the stage reaction from Eq. 3 solely to determine c_{1u}, in the SLC turbine model it is a post-processing parameter defined as $R = h_{\text{blade}}/h_{\text{t,stage}}$.

	Literature	Meanline	SLC
$\dot{m}_{\text{i}}$ [kg/s]	26.26	26.26	26.59 (1.3%)
P [MW]	8.75	8.75	8.57 (-2.1%)
$p_{\text{t,i}}/p_{\text{t,o}}$ [-]	2.25	2.29 (1.8%)	2.29 (1.8%)
R [-]	0.34	0.34	0.38 (11.7%)
Ψ [-]	1.48	1.48 (0.0%)	1.41 (-4.7%)

TABLE 1: Comparison of turbine performance parameters between the meanline and streamline curvature modeling, and the literature [50].

At airfoil level, the comprehensive validation of the thermal model by *Schöffler* [71] against conjugate heat transfer (CHT) high-fidelity calculations is here briefly complemented with the NASA E3 GE HPT first blade. Fig. 4 compares the mid section metal surface temperature between the thermal model discussed in Sec. 2.3.2 and the literature [50]. There is a good agreement at the leading edge with a visible temperature peak in both cases. This is a combination of the high heat transfer coefficient at the stagnation point with the placement of the showerhead holes slightly downstream. Furthermore, the high curvature at the leading edge reduces the internal surface area along with the heat the coolant can absorb, which drives metal temperatures further up.

Downloaded from asmedigitalcollection.asme.org/GT/proceedings-pdf/GT2026/89817/V011T34A011/7650378/v011t34a011-gt2026-175529.pdf by Deutsches Zentrum für Luft- und Raumfahrt (DLR) user on 20 November 2026

Copyright © 2026 by ASME; reuse license CC-BY 4.0

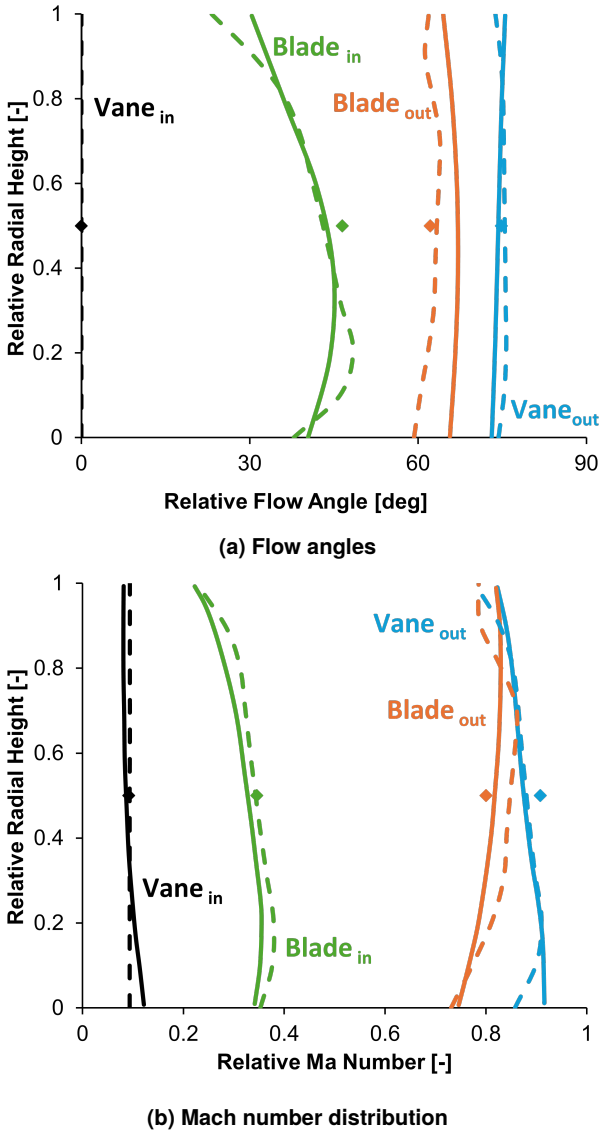

FIGURE 3: Comparison of radial distributions between the mean-line (single point) and streamline curvature modeling (dotted line), and the literature [50] (continuous line).

Both in the pressure side (to the left) and in the suction side (to the right) there is a noticeable temperature over-prediction. In contrast, the suction-side trailing edge shows a noticeable temperature under-prediction. Overall, the predicted temperature profile shows a qualitative agreement with the literature.

It can be challenging to identify the main drivers for the temperature deviations depicted in Fig. 4. Uncertainties at turbine level modeling ultimately affect the hot gas boundary conditions at the airfoil inlet and the Mach number distribution over the airfoil, with a subsequent effect on the film cooling pressure ratios and on the hot gas temperature over the airfoil surface. For example, enforcing a drop in the blade outlet relative Mach number of 0.04 through an artificial blockage factor at the blade throat, similar to the deviation reported in Fig. 3, ultimately results in an average airfoil metal surface temperature deviation of 1 K and a local maximum deviation of 5 K. On the other hand, uncertainties at airfoil level modeling can have a more direct impact on the

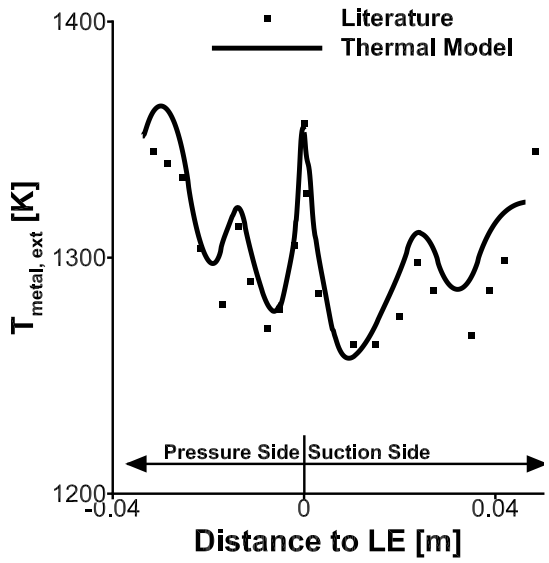

FIGURE 4: Comparison of mid section metal surface temperature at `Take-Off` between the thermal model and the literature [50].

through-wall heat flux and temperature. For example, the thermal model does not yet account for heat transfer between the suction and the pressure side walls at the trailing edge. This correction would lead to a rise in suction-side trailing edge temperature and to a drop in pressure-side trailing edge temperature, bringing the output of the thermal model closer to the literature values. Furthermore, internal heat transfer coefficients are modeled through Nusselt number correlations characterized by a certain level of uncertainty. A representative variation in the multi-pass channel Nusselt number estimation of ± 10%, consistent with the scatter reported by [74], leads to an average airfoil metal surface temperature deviation of 5 K and to a local maximum deviation of 10 K. Finally, external heat transfer coefficients and gas temperature distributions are dependent on the adiabatic film cooling effectiveness, whose predictions are influenced by both correlation accuracy and geometric effects such as surface curvature. A representative variation of ± 20% in suction and pressure-side adiabatic film cooling effectiveness, based on the comparison between correlation and experimental data in [71, 75], results in an average airfoil metal surface temperature deviation of 9 K and a local maximum deviation of 23 K. As a result, we anticipate the temperature deviations from Fig. 4 to be mostly driven by airfoil level and less so by turbine level uncertainties.

Such deviations should not be disregarded, but they are expected and accepted at this low level of fidelity. The presented toolkit and in particular this thermal model is not meant as a replacement for CHT or experimental studies, but instead as a considerable improvement over simple empirical models used at turbine level. Its low computational cost and ease of use enable a rapid generation of different cooling system configurations from scratch and relative analysis between one another. Finally, it should be noted that the deviations discussed above do not constitute a systematic uncertainty quantification, but rather a brief parameter sensitivity assessment. Since the peak deviations are

Downloaded from asmedigitalcollection.asme.org/GT/proceedings-pdf/GT2026/89817/V011T34A011/7650378/v011t34a011-gt2026-175529.pdf by Deutsches Zentrum für Luft- und Raumfahrt (DLR) user on 20 November 2026

Copyright © 2026 by ASME; reuse license CC-BY 4.0

local and may occur at different locations on the airfoil surface, they should not be interpreted as additive contributions to a total temperature uncertainty. While these uncertainties affect absolute temperature values, the discussion in Sec. 3 is focused on relative comparisons between similar cooling system configurations evaluated with the same modeling toolkit from engine to turbine to airfoil. As a result, the trends and the conclusions are expected to be robust.

3. PRE-DESIGN PROCESS

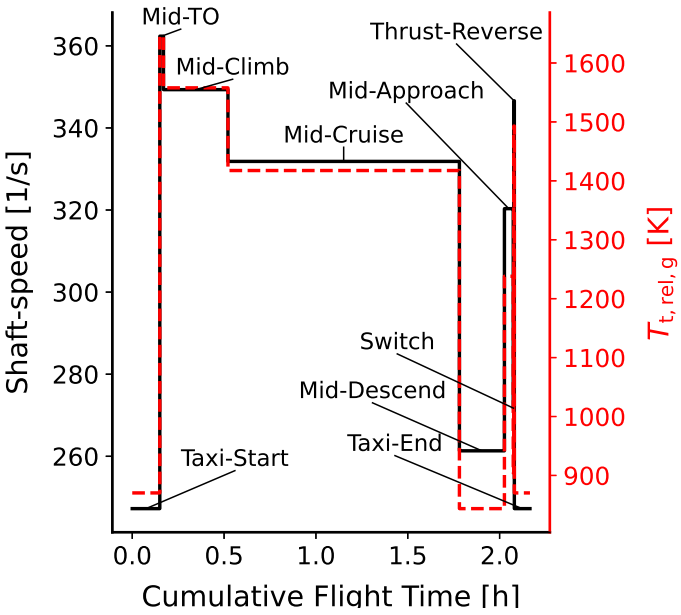

FIGURE 5: Flight cycle D239 with shaft-speed and blade inlet temperature data [43, 44].

The design process presented in the previous section was applied to the first blade of a two-stage HPT in a geared turbo-fan engine of a mid-range commercial platform, depicted in Fig. 2. The engine provides the boundary conditions for the turbine level modeling which in turn provides the boundary conditions for the airfoil level modeling. The design process of the cooled blade accounts for the complete flight envelope. This includes two sets of operating points. The first set consists of requirement operating points (OPs) with corner points (`MTO-SLS`, `EOF` and `TOC`) and an aerodynamic design point (ADP) (`Cruise`). These are rarely flown or not flown at all. The second set of operating points belongs to a particular flight cycle (mission) and represents operating points that are actually flown. This second set includes points such as `Mid-TO` or `Mid-Cruise` that should not be mistaken for the requirement corner OPs or the ADP, as they are always flight cycle specific. In this section, we will refer to requirement OPs, to flight cycle OPs and to the sum of both as the flight envelope OPs. In this demonstration, we accounted for the flight cycle D239 from [43–45] depicted in Fig. 5, roughly equivalent to a flight between Berlin and Barcelona. The operating points in this flight cycle were calculated with standard ISA atmospheric conditions, so the effect of particularly hot regions is currently not accounted for.

After optimizing a turbine geometry with the meanline code for the aerodynamic design point (`Cruise`), both the turbine and

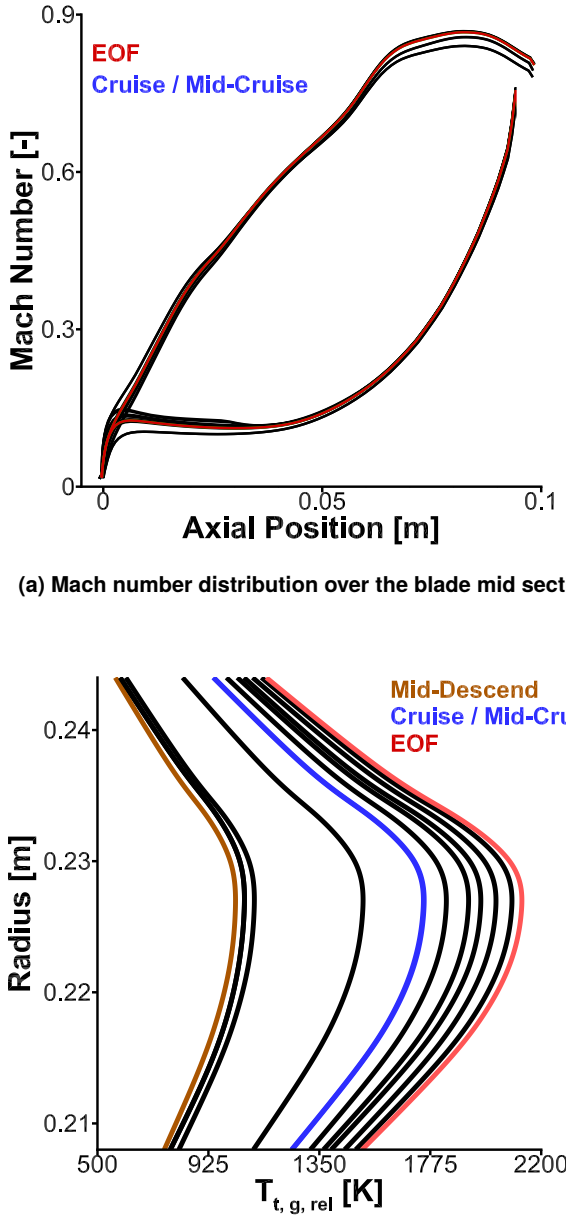

(a) Mach number distribution over the blade mid section

(b) Blade inlet relative total temperature

FIGURE 6: External flow for the first HPT blade throughout the flight envelope.

each turbine row passage flow are recalculated for each operating point in the flight envelope. The output from this step serves as input for the airfoil cooling system modeling and it is partially depicted in Fig. 6. The variation on Mach number distribution over the first HPT blade remains low throughout the flight envelope and should have a small effect on the cooling system performance. On the other hand, the boundary conditions delivered by the SLC turbine model for this first HPT blade vary significantly throughout the flight envelope with a factor of roughly 2.1 between the lowest temperature values experienced at `Mid-Descend` and the highest values at `EOF`. A wide range is also visible for hot gas total pressure and for the coolant state, which will have a significant impact on the cooling system performance.

Downloaded from asmedigitalcollection.asme.org/GT/proceedings-pdf/GT2026/89817/V011T34A011/7650378/v011t34a011-gt2026-175529.pdf by Deutsches Zentrum für Luft- und Raumfahrt (DLR) user on 20 November 2026

Copyright © 2026 by ASME; reuse license CC-BY 4.0

The blade is modeled with the state-of-the-art materials listed in Tab. 2. The third generation CMSX-10 superalloy as base material and the EB-PVD partially Y_2O_3 stabilized ZrO_2 (PYSZ) as thermal barrier coating (TBC).

TABLE 2: Material properties for cooling system analysis [76–82].

Material	T_{max} [K]	λ [W/mK]	YS [MPa]	α [10^{-6} K^{-1}]	ν [-]	E [GPa]
CMSX-10	1323	21.1‡	959‡	13.7‡	0.402‡	98.7‡
TBC	1523	1.54‡	-	-	-	-

The blade cooling system was designed within the constraint space listed in Tab. 3. A maximum coolant-to-mainstream pressure ratio of 0.94 is sufficient to avoid any risk of backflow in the film cooling holes and lies within the typical range of coolant over-pressures reported for turbine airfoils to maintain positive discharge through the film holes and avoid hot gas ingestion [83]. A limit is also set on the Reynolds number for each distinct cooling feature. The impingement jet diameter, the channel hydraulic diameter and the pin diameter are used as characteristic lengths to calculate Re_{jet}, Re_{ch} and Re_{pin}, respectively. The intention for setting these limits is mainly to remain within the valid correlation range and contain modeling uncertainty. Furthermore, very low Reynolds numbers may lead to higher particulate deposition (sand or dust) in multi-pass channel and impingement cooling configurations [84, 85] and very high Reynolds number to more pronounced cold spots in impingement cooling configurations, along with increased thermal stress and coating cracking [86, 87].

TABLE 3: Design constraints enforced throughout the flight envelope.

Criterion	Limit
Film cooling hole pressure ratio (PR_{film})	< 0.94
Channel Reynolds number (Re_{ch})	$10^4 < Re < 10^5$
Jet Reynolds number (Re_{jet})	$5 \times 10^3 < Re < 4 \times 10^4$
Pin Reynolds number (Re_{pin})	$10^3 < Re < 10^5$
Metal temperature (T_{metal})	< 1323 K
Coating temperature (T_{coat})	< 1523 K
Von Mises safety factor (SF_{vM})	> 1.30
Equivalent mission life	$> 1.50 \times 10^4$

The coating temperature is limited to prevent any phase changes and sintering [88]. In addition to the von Mises safety factor limit for instantaneous stress margins, we impose a maximum metal temperature limit to reduce precipitation of TCP phases and γ' coarsening [89]. 1323 K is indeed an aggressive limit, but results will show this is only briefly reached during take-off with maximum metal temperatures dropping to below 1190 K for the remainder of the flight cycle, so that long exposure in this more aggressive degradation regime is avoided. Finally, an equivalent mission life, based on creep damage, is estimated and imposed as a final design constraint. Although absolute creep life is challenging to predict at this level of detail, this metric provides a basis for comparing and selecting an optimum cooling design.

With the set constraints, two separate cooling system configurations were initially generated and compared against one another.

‡Temperature dependent. Value given at 1000K

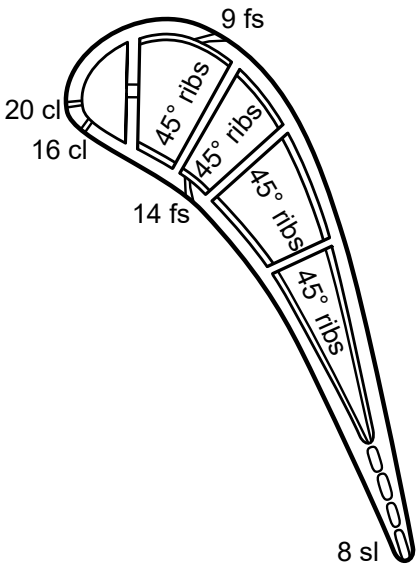

(a) Mid section internal cooling features with blade film cooling hole count; cylindrical (cl), fan-shaped (fs) or slot (sl)

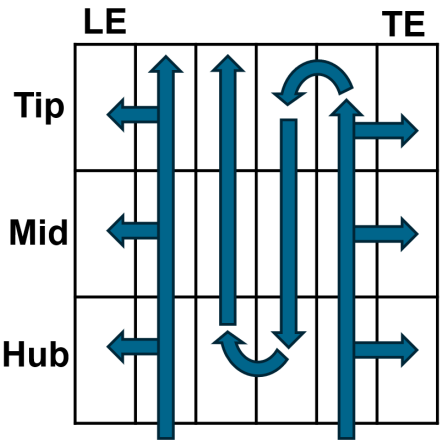

(b) Internal flow path

FIGURE 7: Blade cooling system.

The first, shown in Fig. 7 and Fig. 9, includes an impingement and a feeding channel at the leading edge (LE) and a pin-fin field at the trailing edge (TE) with a ribbed multi-pass channel in between. The second configuration replaces the impingement and the feeding channel with a single LE ribbed channel. The impingement cooling led to an increased heat transfer at the leading edge of the first configuration and to a subsequent reduction in film cooling demand. As a result, the design configuration from Fig. 7 was selected for optimization and iteration with the turbine and engine models. The optimizer was given 53 geometric parameters defining the cooling features throughout the airfoil cooling system and a single fitness function to minimize coolant mass flow, as shown in Fig. 8 for a representative design iteration. Each point signifies a blade cooling system design that has been calculated for the complete flight envelope and that fulfills the design constraints from Tab. 3 at all operating points.

Copyright © 2026 by ASME; reuse license CC-BY 4.0

Downloaded from asmedigitalcollection.asme.org/GT/proceedings-pdf/GT2026/89817/V011T34A011/7650378/v011t34a011-gt2026-175529.pdf by Deutsches Zentrum für Luft- und Raumfahrt (DLR) user on 20 November 2026

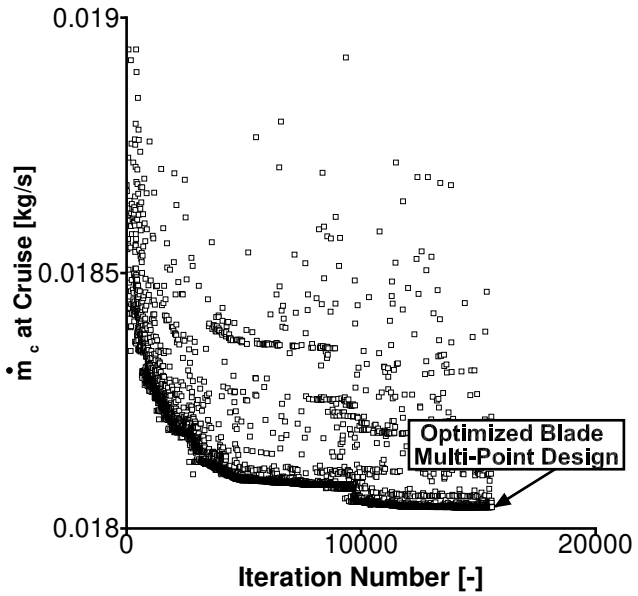

FIGURE 8: Convergence history of multi-point (MP) blade cooling system design optimization. Coolant mass flow is given per blade and at `Cruise` conditions.

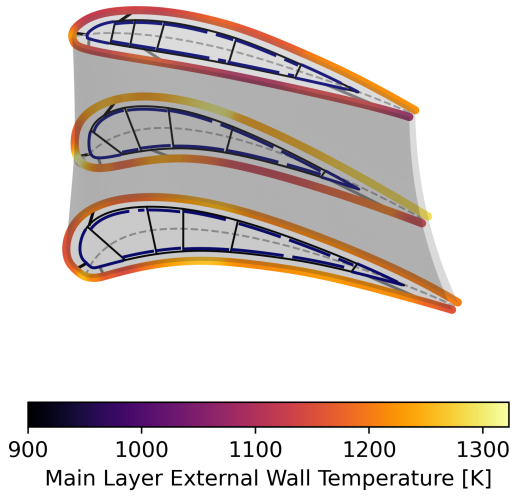

FIGURE 9: Metal surface temperature distribution of multi-point blade cooling system design at `EOF` conditions.

Fig. 10 summarizes the performance of the optimized blade cooling system and shows how the constraints evolve throughout the flight envelope. These constraints are normalized with the values from Tab. 3. The lower bound values for the normalization of the film pressure ratio and the material temperatures are set to the minimum peak values throughout the flight envelope and have no dimensioning meaning. The same is true for the upper bound of the von Mises safety factor normalization. The peak values represent the maximum local value for the specific property throughout the airfoil cooling system. For example, the peak metal temperature at `EOF` conditions shown in Fig. 10 corresponds to the peak temperature at the blade mid section leading edge and suction side, visible in Fig. 9. The Reynolds numbers are given as a range between all of the matrix node values of any one cooling geometry type. The relative damage based on which the mission life is calculated is also depicted to understand the contribution of each flight cycle operating point. Finally, we distinguish between the flight cycle operating points, to the left, and the requirement operating points, to the right.

The film cooling pressure ratio remains quite stable with a maximum of 0.90 at `Thrust-Reverse` and `Mid-Approach`. As a result this does not seem to be a dimensioning factor for the blade cooling system, in contrast to an NGV cooling system where the backflow margin is much tighter.

The Reynolds number in the multi-pass ribbed channels reaches the lower limit at `Mid-Descend`, followed by `Taxi-Start` and `Taxi-End`. Since these are low altitude operating points, it is important to enforce this Reynolds number constraint to avoid a cyclic particle deposition in harsh environments. In the multi-pass and impingement channels, the upper limit is also reached at `Mid-TO` conditions.

Both the coating and metal reach their upper temperature limit at `EOF`, directly followed by `MTO-SLS`, and a minimum of 711 K and 690 K respectively at `Mid-Descend`. In both cases the material temperature varies by a factor of roughly 2 between minimum and maximum peak values. `EOF` is also the operating point with the lowest von Mises safety factor. This comes as a result of the low altitude and high engine load conditions that drive up heat transfer coefficients along with the through-wall heat flux and thermal stress. The shaft-speed and thus centrifugal stress also peak at this operating point so that `EOF` dimensions the cooling system in terms of metal and coating temperatures as well as instantaneous stress margins.

Since neither `EOF` nor `MTO-SLS` actually have any flight time, they do not play a role in terms of creep damage. The resulting equivalent mission life of 1.51×10^4 is a dimensioning parameter mostly through the `Mid-TO` and `Mid-Climb` operating points, followed by `Mid-Cruise` with a minimal contribution. The low impact of `Mid-Cruise` on the creep damage is a combination of the low gas temperature and shaft-speed, that leads to a lower thermal and mechanical stress on the blade, with the short flight time in the current flight cycle.

TABLE 4: Performance comparison between a multi-point (MP) and a single-point (SP) blade cooling system design at `Cruise` conditions.

MP	SP	$\frac{\dot{m}_{c,\,row}}{\dot{m}_{g,\,i,\,row}}$ [-]	η_{TS} [-]	TSFC [g/kNs]	Engine Weight [kg]
x	-	0.0724	0.9013	14.580	2851
-	x	0.0623	0.9050	14.531	2805

To summarize, the blade cooling system is dimensioned by a series of multi-disciplinary aspects that appear throughout the flight envelope and not only at `MTO-SLS` conditions. Enforcing all these constraints in a multi-point (MP) cooling system design drives up the coolant requirements but increases robustness. As a reference, we modeled a separate single-point (SP) cooling system design where the constraints from Tab. 3 were only enforced at `MTO-SLS`. The constraint distribution on the optimized SP design is also depicted in Fig. 10. The film cooling pressure

Downloaded from asmedigitalcollection.asme.org/GT/proceedings-pdf/GT2026/89817/V011T34A011/7650378/v011t34a011-gt2026-175529.pdf by Deutsches Zentrum für Luft- und Raumfahrt (DLR) user on 20 November 2026

Copyright © 2026 by ASME; reuse license CC-BY 4.0

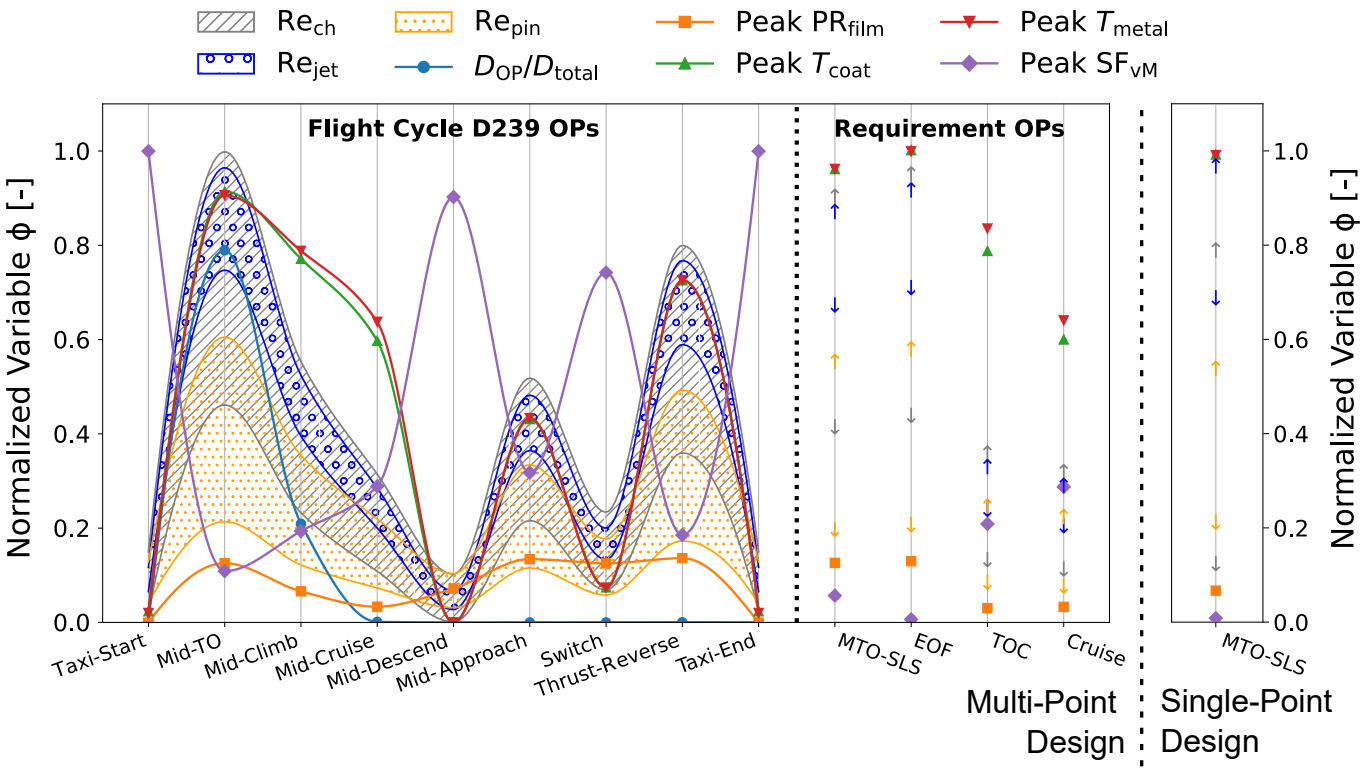

FIGURE 10: To the left: Design constraints for the multi-point cooling system design throughout the flight envelope. This includes the flight cycle D239 with the corresponding operating points and the requirement operating points. Connecting lines use PCHIP interpolation between OPs for visual aid only and lack physical significance. To the right: Design constraints for the single-point cooling system design at `MTO-SLS`.

ratio remains well below the set limit of 0.94 and once again does not dimension the cooling system. In addition, in the SP design the temperature and the von Mises safety factor can reach the limits from Tab. 3 at the stagnation point directly at `MTO-SLS` and as a result the leading edge requires 6.3% less film cooling, in terms of combined cross-sectional area. The same is true for the suction side. Since the suction side wall temperature can reach the limits from Tab. 3 at `MTO-SLS`, the SP design requires less coolant for this region. In particular, it requires 11.1% less film cooling on the suction side and 13.5% less film cooling on the pressure side. The former impacts the suction side external heat transfer coefficient and gas temperature distribution while the latter impacts the suction side internal heat transfer coefficient as it dictates the mass flow through the multi-pass channels. This reduction in pressure-side film cooling is only possible in the SP design because constraint violations due to low Reynolds number at other operating points are not taken into account. Finally, when comparing the optimized MP and SP designs from airfoil to engine through the values given in Tab. 4 for `Cruise` conditions, we see that the MP design results in a 16.2% increase in coolant demand over the SP design, formulated here as the row coolant requirement relative to the row inlet mass flow. At turbine level, the higher mixing losses result in a lower turbine isentropic efficiency. At engine level, the lower turbine efficiency and the higher coolant requirements result in a larger engine core for constant thrust requirements. By keeping a constant fan diameter, the bypass ratio decreases and the TSFC rises. This should not be interpreted negatively, but instead as a trade-off between performance and design robustness. The coolant reduction in the SP design only appears by disregarding critical aspects at other operating points in the flight envelope. The SP blade will generally run hotter than the MP blade throughout the flight envelope, in particular at `EOF`, `Mid-MTO` and `Mid-Climb`, which will lead to a drop in instantaneous stress margins and equivalent mission life to values below those listed in Tab. 3.

So far we discussed savings through uncertainty reduction, the main focus of this paper. A possible next step to increase savings further could be to adopt a variable cooling system throughout the flight envelope [90]. The use case discussed thus far delivers a generally constant relative coolant mass flow throughout the flight envelope. Neither `Cruise` nor `Mid-Cruise` dimension the cooling system in any way, but must currently operate with the unnecessarily high coolant mass flow. This is a considerable loss since `Mid-Cruise` constitutes the majority of the flight cycle operating time. Coolant mass flow at any operating point is set by the blade cooling system design, that defines the combined exit area to the main stream flow through the film cooling holes, and the pressure ratio between coolant and mainstream flow. While the former (the blade cooling system design) cannot change between operating points, the latter (the pressure ratio) could with a variable secondary-air-system [91]. At `Mid-Cruise` conditions, the coolant inlet total pressure could potentially drop by 8.2% before the pressure ratio constraint from Tab. 3 is reached. This would result in a 19.7% drop in coolant mass flow at this operating point. Future analysis will focus on understanding the feasibility and quantifying the impact of such a variable secondary-air-system at turbine and engine level.

Copyright © 2026 by ASME; reuse license CC-BY 4.0

Downloaded from asmedigitalcollection.asme.org/GT/proceedings-pdf/GT2026/89817/V011T34A011/7650378/v011t34a011-gt2026-175529.pdf by Deutsches Zentrum für Luft- und Raumfahrt (DLR) user on 20 November 2026

4. CONCLUSIONS

An established turbine pre-design toolkit was extended in this paper for a multi-point pre-design approach. Following a discussion on each modeling stage and an additional validation with the NASA E3 GE high-pressure turbine, the toolkit was applied to a geared turbofan engine directed at commercial use. A brief analysis, focused on the first high-pressure turbine blade, demonstrated how different constraints appear throughout the flight envelope and impact this particular cooling system design:

- Film-cooling pressure ratio remains below a defined limit of 0.94 across the flight envelope with a maximum of 0.90 at `Thrust-Reverse` and `Mid-Approach`. This is therefore not a sizing parameter.
- Upper Reynolds number limits of 4×10^4 and 10^5 are reached for both impingement and multi-pass ribbed channels respectively at `Mid-TO`. The lower Reynolds number limit of 10^4 is also reached for the multi-pass ribbed channels at `Mid-Descend` conditions. Thus, multi-pass ribbed channel and impingement channel Reynolds numbers are dimensioning parameters for the cooling system at `Mid-TO` and `Mid-Descend`.
- The metal and coating temperature limits of 1323 K and 1523 K as well as the von Mises safety factor limit of 1.3 are reached at `EOF` and are dimensioning parameters at that operating point.
- Creep damage is dominated by `Mid-TO` and `Mid-Climb` with a negligible influence from `Mid-Cruise`.

Comparing a multi-point with a single-point cooling system design shows that sizing the cooling system for the complete flight envelope increases coolant requirements by 16.2% relative to a single-point design, but simultaneously ensures that thermal and structural limits are satisfied across all operating points. In practical terms, this means that the single-point design may either experience premature failure if a coolant safety margin is set below 16.2%, or incur unnecessary TSFC penalties if the set margin exceeds this value. The multi-point design approach therefore achieves a more favorable balance between cooling system design robustness and fuel consumption.

Going one step forward, a brief analysis motivates a variable secondary-air-system capable of modulating coolant air pressure to reduce coolant mass flow on non-dimensioning operating points. In the current case, for example at `Mid-Cruise` conditions, a drop in coolant inlet total pressure of 8.2% is allowed within the constraint space and would lead to a 19.7% reduction in coolant mass flow.

This pre-design process lays the basis for feasibility and potential benefit studies on use cases with variable secondary-air-systems as well as for design tasks with wider flight envelopes or with multiple flight cycles. It also enables studies on different material and cooling technologies throughout various use cases.

Each of the discussed modeling stages is naturally affected by errors due to the correlation based nature of pre-design methods. A next step includes an analysis between engine, turbine and airfoil modeling to understand how the compounded errors affect the final cooling system design. This will also help determine which modeling steps have the highest sensitivity on the cooling system and where development should be invested. Finally, the preliminary structural analysis should be extended to include additional stress components and validated against high-fidelity data. The subsequent damage analysis, currently available for creep, should be extended where possible to account for oxidation and fatigue.

ACKNOWLEDGMENTS

The presented results have been developed in close cooperation with the partners of the DLR projects FFE+, 3DCeraTurb, ADAPT and InnoCool.

REFERENCES

[1] Padture, N. "Advanced Structural Ceramics in Aerospace Propulsion." *Nature Materials* Vol. 15 No. 8 (2016): pp. 804–809. DOI 10.1038/nmat4687.

[2] Cumpsty, N. and Heyes, A. *Jet Propulsion*. Cambridge University Press, Cambridge (2015).

[3] Braeunling, W. *Flugzeugtriebwerke: Grundlagen, Aero-Thermodynamik, ideale und reale Kreisprozesse, thermische Turbomaschinen, Komponenten, Emissionen und Systeme*. Springer Vieweg, Berlin (2015).

[4] Horlock, J., Watson, D. and Jones, T. "Limitations on Gas Turbine Performance Imposed by Large Turbine Cooling Flows." *Journal of Engineering for Gas Turbines and Power* Vol. 123 No. 3 (2001): pp. 487–494. DOI 10.1115/1.1373398.

[5] Carvalho, F., Wehrel, P., Matuschek, T., Schöffler, R., Brakmann, R., Behrendt, T., Ebel, P., Schulz, U. and Herbst, F. "Pre-Design and Analysis of a Military Hybrid High-Pressure Turbine." *Journal of Engineering for Gas Turbines and Power* Vol. 148 No. 4 (2026): p. 041023. DOI 10.1115/1.4069736.

[6] "RTX's Pratt & Whitney Announces GTF Hot Section Plus." (2025). Accessed 2025-03-12, URL https://www.rtx.com/news/news-center/2025/06/16/rtxs-pratt-whitney-announces-gtf-hot-section-plus.

[7] Stubbins, G. "CFM International Reaches Milestones for LEAP Engine Maturity." (2025). Accessed 2025-03-12, URL https://www.compositesworld.com/news/cfm-international-reaches-milestones-for-leap-engine-maturity.

[8] Perry, D. "Rolls-Royce Trusts in Dust as Trent XWB-97 Durability Upgrades 'Exceed Expectations' in Testing." (2025). Accessed 2025-03-12, URL https://www.flightglobal.com/engines/rolls-royce-trusts-in-dust-as-trent-xwb-97-durability-upgrades-exceed-expectations-in-testing/165291.article.

[9] Grieb, H. *Projektierung von Turboflugtriebwerken*. Springer, Basel (2004). DOI 10.1007/978-3-0348-7938-5.

[10] Seitz, A. "Advanced Methods for Propulsion System Integration in Aircraft Conceptual Design." Ph.D. Thesis, Technische Universität München. 2012.

[11] Young, J. and Wilcock, R. "Modeling the Air-Cooled Gas Turbine: Part 2 - Coolant Flows and Losses." *Journal of Turbomachinery* Vol. 124 No. 2 (2002): pp. 214–221. DOI 10.1115/1.1415038.

Copyright © 2026 by ASME; reuse license CC-BY 4.0

Downloaded from asmedigitalcollection.asme.org/GT/proceedings-pdf/GT2026/89817/V011T34A011/7650378/v011t34a011-gt2026-175529.pdf by Deutsches Zentrum für Luft- und Raumfahrt (DLR) user on 20 November 2026

[12] Holland, M. and Thake, T. "Rotor Blade Cooling in High Pressure Turbines." *Journal of Aircraft* Vol. 17 No. 6 (1980): pp. 412–418. DOI 10.2514/3.44668.

[13] Jonsson, M. and Bolland, O. "Gas Turbine Cooling Model for Evaluation of Novel Cycles." *Proceedings of ECOS 2005*. 2005. Trondheim, Norway.

[14] Lallini, V., Janikovic, J., Pilidis, P., Singh, R. and Laskaridis, P. "A Calculation Tool of a Turbine Cooling Air Schedule for General Gas Turbine Simulation Algorithms." *Journal of Turbomachinery* Vol. 134 No. 4 (2012): p. 041003. DOI 10.1115/1.4003648.

[15] Uysal, S., Liese, R., Nix, A. and Black, J. "A Thermodynamic Model to Quantify the Impact of Cooling Improvements on Gas Turbine Efficiency." *Proceedings of the ASME Turbo Expo 2017*. 2017. American Society of Mechanical Engineers, Charlotte, North Carolina, USA. DOI 10.1115/GT2017-63480.

[16] Carvalho, F., Wehrel, P., Grunwitz, C., Schöffler, R. and Brakmann, R. "Cooling Model Calibration in a Collaborative Turbine Preliminary Design Process Using the NASA Energy Efficient Engine - Part II: 1D Turbine Modeling." *International Journal of Gas Turbine, Propulsion and Power Systems* Vol. 15 No. 3 (2024): pp. 31–41. DOI 10.38036/jgpp.15.3_31.

[17] Wehrel, P., Schöffler, R., Grunwitz, C., Carvalho, F., Plohr, M., Häßy, J. and Petersen, A. "Performance and Emissions Benefits of Cooled Ceramic Matrix Composite Vanes for High-Pressure Turbines." *Journal of Engineering for Gas Turbines and Power* Vol. 145 No. 12 (2023): p. 121016. DOI 10.1115/1.4063534.

[18] Görtz, A. and Schneider, B. "Step-by-Step Evaluation of the Fuel Switch From Kerosene to Hydrogen on the Thermodynamic Cycle in Gas Turbine Engines." *Journal of Engineering for Gas Turbines and Power* Vol. 146 No. 11 (2024): p. 111015. DOI 10.1115/1.4065926.

[19] Schmeink, J., Görtz, A. and Häßy, J. "Application of a Global Sensitivity Screening Method for Design Space Exploration of Coupled Turbofan Engine Performance and Preliminary Design." *GPPS*. 2020. DOI 10.33737/gpps20-tc-71.

[20] Fröhler, B., Häßy, J. and Abu-Zurayk, M. "Development of a Medium/Long-Haul Reference Aircraft." *CEAS Aeronautical Journal* Vol. 14 No. 3 (2023): pp. 693–713. DOI 10.1007/s13272-023-00662-1.

[21] Schneider, B. "Turbine Cooling Air Estimation in Thermodynamic Simulations." *CEAS Aeronautical Journal* Vol. 16 No. 1 (2025): pp. 141–156. DOI 10.1007/s13272-024-00776-0.

[22] Bijewitz, J., Seitz, A. and Hornung, M. "Power Plant Pre-Design Exploration for a Turbo-Electric Propulsive Fuselage Concept." *2018 Joint Propulsion Conference*. 2018. American Institute of Aeronautics and Astronautics, Cincinnati, Ohio, USA. DOI 10.2514/6.2018-4402.

[23] Pohl, M., Köhler, J., Kellermann, H., Lüdemann, M., Weintraub, D., Jeschke, P. and Hornung, M. "Preliminary Design of Integrated Partial Turboelectric Aircraft Propulsion Systems." *Journal of the Global Power and Propulsion Society* Vol. 6 (2022): pp. 1–23. DOI 10.33737/jgpps/145907.

[24] Ziegler, P., Kaiser, S. and Gümmer, V. "Parametric Cycle Studies of the Water-Enhanced Turbofan Concept." *Proceedings of ASME Turbo Expo 2023*. 2023. American Society of Mechanical Engineers, Boston, Massachusetts, USA. DOI 10.1115/GT2023-100529.

[25] Searle, M., Roy, A., Ramesh, S., Floyd, T., Ames, F. and Straub, D. "Novel Additively-Manufactured and Internally-Cooled Airfoils for Increasing Small Industrial Gas Turbine Efficiency." *Proceedings of ASME Turbo Expo 2023*. 2023. Boston, Massachusetts, USA. DOI 10.1115/GT2023-101006.

[26] Poupinha, C., Kozlowska, S., Lluch, J., Altimare, D. and Kinell, M. "Experimental Study on Transpiration Cooling through Additively Manufactured Porous Structures." *International Journal of Heat and Mass Transfer* Vol. 227 (2024): p. 125532. DOI 10.1016/j.ijheatmasstransfer.2024.125532.

[27] Ngetich, G., Ireland, P., Murray, A. and Romero, E. "A 3D Conjugate Approach for Analysing a Double-Walled Effusion-Cooled Turbine Blade." *Proceedings of ASME Turbo Expo 2018*. 2018. Oslo, Norway. DOI 10.1115/GT2018-76534.

[28] Du, H., Mei, Z., Zou, J., Jiang, W. and Xie, D. "Conjugate Heat Transfer Investigation on Swirl-Film Cooling at the Leading Edge of a Gas Turbine Vane." *Entropy* Vol. 21 No. 10 (2019): p. 1007. DOI 10.3390/e21101007.

[29] Woelki, D. and Peitsch, D. "A Framework for Applied Component Zooming in Gas Turbines." *Proceedings of the DLRK 2020*: p. 16 pages. 2020. Deutsche Gesellschaft für Luft- und Raumfahrt - Lilienthal-Oberth e.V. DOI 10.25967/490174.

[30] Schuff, M. "Towards Multi-Fidelity Simulations in the Context of the Virtual Engine." *Proceedings of the DLRK 2024*: p. 10 pages. 2024. Deutsche Gesellschaft für Luft- und Raumfahrt - Lilienthal-Oberth e.V. DOI 10.25967/610297.

[31] Yin, F., Tiemstra, F. and Rao, A. "Development of a Flexible Turbine Cooling Prediction Tool for Preliminary Design of Gas Turbines." *Journal of Engineering for Gas Turbines and Power* Vol. 140 No. 9 (2018): p. 091201. DOI 10.1115/1.4039732.

[32] Schroeter, J., Armbrüster, F., Schaber, R. and Gümmer, V. "Optimization of a Battery Electric Hybrid Propulsion System for a Short Range Aircraft." *Proceedings of ASME Turbo Expo 2024*. 2024. American Society of Mechanical Engineers, London, United Kingdom. DOI 10.1115/GT2024-125840.

[33] Müller, M., Schöffler, R., Grunwitz, C. and Morsbach, C. "Modelling the Film Cooling of a Modern High-Pressure Turbine Nozzle Guide Vane in 3D CFD." *Proceedings of ASME Turbo Expo 2024*. 2024. American Society of Mechanical Engineers, London, United Kingdom. DOI 10.1115/GT2024-126684.

[34] Schöffler, R., Grunwitz, C. and Brakmann, R. "A Semi-Empirical Model for Conceptual Turbine Vane Cooling

Downloaded from asmedigitalcollection.asme.org/GT/proceedings-pdf/GT2026/89817/V011T34A011/7650378/v011t34a011-gt2026-175529.pdf by Deutsches Zentrum für Luft- und Raumfahrt (DLR) user on 20 November 2026

Copyright © 2026 by ASME; reuse license CC-BY 4.0

Design and Optimization." *Proceedings of ASME Turbo Expo 2023*. 2023. American Society of Mechanical Engineers, Boston, Massachusetts, USA. DOI 10.1115/GT2023-103061.

[35] Schöffler, R., Müller, M., Grunwitz, C., Brakmann, R. and Krewinkel, R. "Potential of a Nozzle Guide Vane Cooling Concept Adapted to Circumferential Temperature Variations." *Proceedings of ASME Turbo Expo 2025*. 2025. American Society of Mechanical Engineers, Memphis, Tennessee, USA. DOI 10.1115/GT2025-152700.

[36] Girardeau, J., Pailhes, J., Sebastian, P., Pardo, F. and Nadeau, J. "Turbine Blade Cooling System Optimization." *Journal of Turbomachinery* Vol. 135 No. 6 (2013): p. 061020. DOI 10.1115/1.4023466.

[37] Town, J., Straub, D., Black, J., Thole, K. and Shih, T. "State-of-the-Art Cooling Technology for a Turbine Rotor Blade." *Journal of Turbomachinery* Vol. 140 No. 7 (2018): p. 071007. DOI 10.1115/1.4039942.

[38] Kaufman, A. and Gaugler, R. "Thermal-Structural Mission Analyses of Air-Cooled Gas Turbine Blades." *Proceedings of the ASME Turbo Expo 1979*. 1979. American Society of Mechanical Engineers, San Diego, California, USA. DOI 10.1115/79-GT-19.

[39] Van Enkhuizen, M., Dresbach, C., Reh, S. and Kuntzagk, S. "Efficient Lifetime Prediction of High Pressure Turbine Blades in Real Life Conditions." *Proceedings of ASME Turbo Expo 2017*. 2017. American Society of Mechanical Engineers, Charlotte, North Carolina, USA. DOI 10.1115/GT2017-63341.

[40] Cheng, M., Yang, X., Fan, Y, Sun, Y., Ji, P. and Shi, D. "A Comprehensive Computational Framework for Damage Assessment of Turbine Blades Considering Multidamage Mechanism and Service History." *Fatigue & Fracture of Engineering Materials & Structures* Vol. 48 No. 8 (2025): pp. 3398–3415. DOI 10.1111/ffe.14677.

[41] Grunwitz, C., Brose, N., Schöffler, R. and Carvalho, F. "A Comprehensive Multifidelity Design and Analysis Process for Cooled Axial Flow Turbines: From Concept to Component." *Proceedings of the International Gas Turbine Congress 2023*. 2023. Kyoto, Japan. DOI 10.58114/BDXV-4521.

[42] Reitenbach, S., Vieweg, M., Becker, R., Hollmann, C., Wolters, F., Schmeink, J., Otten, T. and Siggel, M. "Collaborative Aircraft Engine Preliminary Design Using a Virtual Engine Platform, Part A: Architecture and Methodology." *AIAA Scitech 2020 Forum*. 2020. American Institute of Aeronautics and Astronautics, Orlando, USA. DOI 10.2514/6.2020-0867.

[43] Hässy, J. and Schmeink, J. "Knowledge-Based Conceptual Design Methods for Geometry and Mass Estimation of Rubber Aero Engines." *33rd Congress of the International Council of the Aeronautical Sciences*. 2022. Stockolm, Sweden.

[44] Wöhler, S., Hässy, J. and Kriewall, V. "Establishing the DLR-F25 as a Research Baseline Aircraft for the Short-Medium Range Market in 2035." *34th Congress of the International Council of the Aeronautical Sciences*. 2024. Florence, Italy.

[45] Wehrel, P., Carvalho, F., Schmeink, J. and Häßy, J. "Multidisciplinary Lifetime Assessement of Turbine Rotors and Disks from a Conceptual Engine Design Perspective." *Proceedings of ASME Turbo Expo 2026*. 2026. Milan, Italy.

[46] Krumme, A. "Konzeption, Implementierung Und Anwendung Eines Automatisierten Aerothermodynamischen Vorentwurfsprozesses Fuer Axialturbinen." Ph.D. Thesis, Universitaet Kassel. 2015.

[47] Krumme, A. "Performance Prediction and Early Design Code for Axial Turbines and Its Application in Research and Predesign." *Proceedings of ASME Turbo Expo 2016*. 2016. Seoul, South Korea. DOI 10.1115/GT2016-56082.

[48] Ainley, D. and Mathienson, G. "An Examination of the Flow and Pressure Losses in Blade Rows of Axial Flow Turbines." Technical Report No. 2891. London, United Kingdom. 1951.

[49] Zweifel, O. "The Spacing of Turbomachine Blading, Especially with Large Angular Deflection." *The Brown Boveri Review* Vol. 32 (1945): pp. 436–444.

[50] Halila, E., Lenahan, D. and Thomas, T. "Energy Efficient Engine - High Pressure Turbine - Test Hardware Detailed Design Report." Technical Report CR-167955. NASA, Cleveland. 1982.

[51] Thulin, R., Howe, D. and Singer, I. "Energy Efficient Engine - High-Pressure Turbine Detailed Design Report." Technical Report CR-165608. NASA, Cleveland. 1982.

[52] Povey, T and Qureshi, I. "A Hot-Streak (Combustor) Simulator Suited to Aerodynamic Performance Measurements." *Journal of Aerospace Engineering* Vol. 222 No. 6 (2008): pp. 705–720. DOI 10.1243/09544100JAERO363.

[53] Kost, F. "Ein Verfahren Zur Berechnung Der Meridionalstroemung von Axialturbinen." Technical Report No. 225-2014-A-01. DLR, Göttingen. 2014.

[54] Denton, J. "Throughflow Calculations for Transonic Axial Flow Turbines." *Journal of Engineering for Power* Vol. 100 No. 2 (1978): pp. 212–218. DOI 10.1115/1.3446336.

[55] Kacker, S. and Okapuu, U. "A Mean Line Prediction Method for Axial Flow Turbine Efficiency." *Journal of Engineering for Power* Vol. 104 No. 1 (1982): pp. 111–119. DOI 10.1115/1.3227240.

[56] Zhu, J. and Sjolander, S. "Improved Profile Loss and Deviation Correlations for Axial-Turbine Blade Rows." *Proceedings of ASME Turbo Expo 2005*: pp. 783–792. 2005. American Society of Mechanical Engineers, Reno, Nevada, USA. DOI 10.1115/GT2005-69077.

[57] Aungier, R. *Turbine Aerodynamics: Axial-Flow and Radial-Flow Turbine Design and Analysis*. ASME Press, New York (2006). DOI 10.1115/1.802418.

[58] Benner, M., Sjolander, S. and Moustapha, S. "An Empirical Prediction Method For Secondary Losses In Turbines - Part II: A New Secondary Loss Correlation." *Journal of Turbomachinery* Vol. 128 No. 2 (2006): pp. 281–291. DOI 10.1115/1.2162594.

Downloaded from asmedigitalcollection.asme.org/GT/proceedings-pdf/GT2026/89817/V011T34A011/7650378/v011t34a011-gt2026-175529.pdf by Deutsches Zentrum für Luft- und Raumfahrt (DLR) user on 20 November 2026

Copyright © 2026 by ASME; reuse license CC-BY 4.0

[59] Hartsel, J. "Prediction of Effects of Mass-Transfer Cooling on the Blade-Row Efficiency of Turbine Airfoils." *Proceedings of the 10th Aerospace Sciences Meeting*. 1972. San Diego,California, USA. DOI 10.2514/6.1972-11.

[60] Siller, U., Voß, C. and Nicke, E. "Automated Multidisciplinary Optimization of a Transonic Axial Compressor." *47th AIAA Aerospace Sciences Meeting Including The New Horizons Forum and Aerospace Exposition*. 2009. Orlando, Florida, USA. DOI 10.2514/6.2009-863.

[61] Drela, M. and Giles, M. "Viscous-Inviscid Analysis of Transonic and Low Reynolds Number Airfoils." *AIAA Journal* Vol. 25 No. 10 (1987): pp. 1347–1355. DOI 10.2514/3.9789.

[62] Young, Warren Clarence and Budynas, Richard G. *Roark's Formulas for Stress and Strain*, 7th ed. McGraw-Hill, New York (2002).

[63] Kerrebrock, J. *Aircraft Engines and Gas Turbines*. The MIT Press, Cambridge, Massachusetts, USA (1992).

[64] Hertzberg, R., Vinci, R. and Hertzberg, J. *Deformation and Fracture Mechanics of Engineering Materials*, 6th ed. Wiley, Hoboken, NJ (2020).

[65] Xu, Y., Sun, W., Dai, W., Hu, C., Liu, X. and Zhang, W. "Experimental and Numerical Modeling of the Stress Rupture Behavior of Nickel-Based Single Crystal Superalloys Subject to Multi-Row Film Cooling Holes." *Metals* Vol. 7 No. 9 (2017): p. 340. DOI 10.3390/met7090340.

[66] Lukáš, P., Preclík, P. and Čadek, J. "Notch Effects on Creep Behaviour of CMSX-4 Superalloy Single Crystals." *Materials Science and Engineering: A* Vol. 298 No. 1-2 (2001): pp. 84–89. DOI 10.1016/S0921-5093(00)01288-0.

[67] Larson, F. and Miller, J. "A Time-Temperature Relationship for Rupture and Creep Stresses." *Journal of Fluids Engineering* Vol. 74 No. 5 (1952): pp. 765–771. DOI 10.1115/1.4015909.

[68] Miner, M. "Cumulative Damage in Fatigue." *Journal of Applied Mechanics* Vol. 12 No. 3 (1945): pp. A159–A164. DOI 10.1115/1.4009458.

[69] Robinson, E. "Effect of Temperature Variation on the Long-Time Rupture Strength of Steels." *Journal of Fluids Engineering* Vol. 74 No. 5 (1952): pp. 777–780. DOI 10.1115/1.4015916.

[70] Wang, Y., Wang, X., Yang, Y., Lan, X., Zhang, Z. and Li, H. "Study on Creep-Fatigue Mechanical Behavior and Life Prediction of Ti2AlNb-Based Alloy." *Materials* Vol. 15 No. 18 (2022): p. 6238. DOI 10.3390/ma15186238.

[71] Schöffler, R. "Influence of Spatial Turbine Inlet Flow Distortion on the Design of Nozzle Guide Vane Cooling Systems." Ph.D. Thesis, Technische Universität Graz. 2026.

[72] Wehrel, P. and Carvalho, F. "Cooling Model Calibration in a Collaborative Turbine Preliminary Design Process Using the NASA Energy Efficient Engine - Part I: 0D Performance Modeling." *International Journal of Gas Turbine, Propulsion and Power Systems* Vol. 15 No. 3 (2024): pp. 18–30. DOI 10.38036/jgpp.15.3_18.

[73] Krumme, A., Hegen, S. and Nahuis, R. "Design of a Multi-Stage Axial Turbine within the Scope of Complete System Design, Manufacturing and Operation of a New Turbine Propulsion Simulator (TPS)." *33rd AIAA Applied Aerodynamics Conference*. 2015. American Institute of Aeronautics and Astronautics, Dallas, Texas, USA. DOI 10.2514/6.2015-2256.

[74] Han, J. C., Zhang, Y. M. and Lee, C. P. "Augmented Heat Transfer in Square Channels With Parallel, Crossed, and V-Shaped Angled Ribs." *Journal of Heat Transfer* Vol. 113 No. 3 (1991): pp. 590–596. DOI 10.1115/1.2910606. Accessed 2023-01-24, URL https://asmedigitalcollection.asme.org/heattransfer/article/113/3/590/415044/Augmented-Heat-Transfer-in-Square-Channels-With.

[75] Colban, W., Thole, K. and Bogard, D. "A Film-Cooling Correlation for Shaped Holes on a Flat-Plate Surface." *Journal of Turbomachinery* Vol. 133 No. 1 (2011): p. 011002. DOI 10.1115/1.4002064.

[76] Koizumi, Y., Kobayashi, T., Yokokawa, T., Zhang, J., Osawa, M., Harada, H., Aoki, Y. and Arai, M. "Development of Next-Generation Ni-Base Single Crystal Superalloys." *Journal of the Japan Institute of Metals and Materials* Vol. 67 No. 9 (2004): pp. 35–43. DOI 10.7449/2004/Superalloys_2004_35_43.

[77] Rätzer-Scheibe, H.-J. and Schulz, U. "The Effects of Heat Treatment and Gas Atmosphere on the Thermal Conductivity of APS and EB-PVD PYSZ Thermal Barrier Coatings." *Surface and Coatings Technology* Vol. 201 No. 18 (2007): pp. 7880–7888. DOI 10.1016/j.surfcoat.2007.03.028.

[78] Clarke, D., Oechsner, M. and Padture, N. "Thermal-Barrier Coatings for More Efficient Gas-Turbine Engines." *MRS Bulletin* Vol. 37 No. 10 (2012): pp. 891–898. DOI 10.1557/mrs.2012.232.

[79] Erickson, G. "The Development and Application of CMSX-10." Technical report no. TMS. 1996.

[80] Reed, R. *The Superalloys: Fundamentals and Applications*. Cambridge University Press, London, United Kingdom (2006). DOI 10.1017/CBO9780511541285.

[81] Quested, P., Brooks, R., Chapman, L., Morrell, R., Youssef, Y. and Mills, K. "Measurement and Estimation of Thermophysical Properties of Nickel Based Superalloys." *Materials Science and Technology* Vol. 25 No. 2 (2009): pp. 154–162. DOI 10.1179/174328408X361454.

[82] Epishin, A. and Lisovenko, D. "Comparison of Isothermal and Adiabatic Elasticity Characteristics of the Single Crystal Nickel-Based Superalloy CMSX-4 in the Temperature Range Between Room Temperature and 1300°C." *Mechanics of Solids* Vol. 58 No. 5 (2023): pp. 1587–1598. DOI 10.3103/S0025654423601301.

[83] Han, J., Dutta, S. and Ekkad, S. *Gas Turbine Heat Transfer and Cooling Technology*, 2nd ed. CRC Press (2012). DOI 10.1201/b13616.

[84] Kong, D., Tian, X., Li, G., Liu, C., Niu, X., Isaev, S. and Penyazkov, O. "Numerical Study of Particle Deposition and Heat Transfer Characteristics in an S-shaped Miniature Cooling Channel of a Gas Turbine Blade." *Powder Technology* Vol. 468 (2026): p. 121612. DOI 10.1016/j.powtec.2025.121612.

Downloaded from asmedigitalcollection.asme.org/GT/proceedings-pdf/GT2026/89817/V011T34A011/7650378/v011t34a011-gt2026-175529.pdf by Deutsches Zentrum für Luft- und Raumfahrt (DLR) user on 20 November 2026

Copyright © 2026 by ASME; reuse license CC-BY 4.0

[85] Lin, L., Cunliang, L., Wei, L., Webin, C., Huiren, Z. and Weijang, X. "Numerical Research on the Particle Transport and Deposition in the Impingement-Film Cooling Passage." *Physics of Fluids* Vol. 35 No. 5 (2023): p. 053302. DOI 10.1063/5.0147549.

[86] Brakmann, R., Brose, N., Carvalho, F. and Chargui, S. "A Numerical Analysis of Cross-Flow Reinforced Impingement Cooling with a U-Shaped Flow-Guide on the Hole Plate." *Proceedings of ASME Turbo Expo 2023*. 2023. American Society of Mechanical Engineers, Boston, USA. DOI 10.1115/GT2023-101097.

[87] Howell, P., Retting, W., Steinkopff, T., Subramanian, R., Wolff, A. and Lampenscherf, S. "The Influence of Heating and Cooling Rates on TBC Failure in High Heat Flux Tests." (2018). Accessed 2025-08-12, URL https://dc.engconfintl.org/tbcv/55/.

[88] Schulz, U., Fritscher, K., Leyens, C. and Peters, M. "High-Temperature Aging of EB-PVD Thermal Barrier Coatings." Singh, Mrityunjay and Jessen, Todd (eds.). *Ceramic Engineering and Science Proceedings*. Vol. 22. John Wiley & Sons, Inc., Hoboken, New Jersey, USA (2001): pp. 347–356. DOI 10.1002/9780470294703.ch42.

[89] Acharya, M. and Fuchs, G. "The Effect of Long-Term Thermal Exposures on the Microstructure and Properties of CMSX-10 Single Crystal Ni-base Superalloys." *Materials Science and Engineering: A* Vol. 381 No. 1-2 (2004): pp. 143–153. DOI 10.1016/j.msea.2004.04.001.

[90] Pontika, E., Laskaridis, P., Gonzalez, F., Jacobs, W. and Mills, A. "Mapping the Effect of Variable HPT Blade Cooling on Fuel Burn, Engine Life and Emissions for Fleet Optimization Using Active Control." *AIAA SCITECH 2023 Forum*. 2023. American Institute of Aeronautics and Astronautics, National Harbor, Maryland, USA. DOI 10.2514/6.2023-0706.

[91] Woelki, D. and Peitsch, D. "Trade-Off Assessments for Part Load Controlled Cooling Air in Stationary Gas Turbines." *Proceedings of ASME Turbo Expo 2020*: p. V005T06A029. 2020. American Society of Mechanical Engineers, Virtual, Online. DOI 10.1115/GT2020-15670.

Downloaded from asmedigitalcollection.asme.org/GT/proceedings-pdf/GT2026/89817/V011T34A011/7650378/v011t34a011-gt2026-175529.pdf by Deutsches Zentrum für Luft- und Raumfahrt (DLR) user on 20 November 2026

 Copyright © 2026 by ASME; reuse license CC-BY 4.0